



Self-heating in rubber components: experimental studies and numerical analysis

Mohamed Abdelmoniem¹ · Bülent Yagimli¹

Received: 18 October 2023 / Revised: 28 March 2024 / Accepted: 3 April 2024
© The Author(s) 2024

Abstract

The temperature change in rubber components during operation results in a change in its transfer function and affects service life. In this study, the phenomenon of self-heating and its effect on the resulting forces is examined experimentally under different loading conditions using a test rig that applies a rotating shear load. The observed phenomenon from the tests was modelled using a finite viscoelastic model based on the multiplicative decomposition of the deformation gradient. The simulation results of the surface temperature and the resulting forces using the implemented material model showed good agreement with experimental results. The test rig and the simulation model can be used to characterise rubber materials and therefore, allow the prediction of the temperature distribution and the transfer function of rubber components under operational conditions.

Keywords Self-heating · Material modelling · Thermomechanics · Finite element implementation

Introduction

In the development phase of rubber components, two important considerations are considered, viz. its transfer function to other components and how long it will maintain its functionality, i.e., its life cycle. The transfer function and the life cycle are both affected by the self-heating phenomena of rubber materials. In the literature, several experimental investigations and numerical simulations were performed to understand this phenomenon. The self-heating under cyclic loads was studied by Peter et al. [20] for a cylindrical specimen under different rotational speeds using the heat buildup analyser introduced by Stoczek et al. [29]. A numerical approach was suggested, where the dissipation energy is calculated from the strain energy density using a dissipation constant. The dissipation constant and the thermal parameters, such as heat convection coefficient and thermal conductance, were determined so that good agreement with the experiment is achieved. The workflow in [20] was implemented using Ansys Workbench, and the temperature inside and outside the sample corresponds well to the experimental

data. A similar procedure for calculating the self-heat was introduced by Banic et al. [2]. The simulation results were verified against experimental results using an example of a rubber spring subjected to dynamic uniaxial compression loading. For the same loading on the heat build-up analyser, Werner et al. [30] proposed a new approach for simulating the heat build-up while considering the temperature dependence of the mechanical properties. The calculation procedure is performed iteratively, where in the first step, the dissipation due to cyclic loading is obtained and the steady-state temperature is calculated. The average temperature along the rubber cross-section is then used to adjust the mechanical properties for the dissipation calculation in the next iteration.

Cruanes et al. [6] proposed an experimental thermo-mechanical law based on the evolution of the self-heating derivative with respect to the number of cycles during fatigue tests. The proposed law shows a good fit, irrespective of the sample's shape or volume. Demonstrating the self-heating on an example of a solid tyre, He et al. [10] calculated the heat build-up using the Endurica CL workflow [17]. Two simulations are conducted separately, structural analysis and thermal analysis. The structural analysis is used to obtain the strain history which is then provided as an input to the dissipation calculation. In the dissipation calculation, the heat generation rate is estimated from the given strain history using the Kraus model [14]. The dissipation

✉ Mohamed Abdelmoniem
m.abdelmoniem@ostfalia.de

¹ Faculty of Mechanical Engineering, Ostfalia University of Applied Sciences, 38302 Wolfenbüttel, Germany

and the surface temperature are calculated iteratively until a convergence of the temperature results is obtained. The introduced workflow provides simulation results with a good agreement with the test data. Thermomechanical constitutive models describing the dissipation behaviour and self-heating of elastomers were proposed by Lion [16], Reese and Govindjee [21], Behnke et al. [4] and Boukamel et al. [5]. In the work by Rodas et al. [24], a finite viscoelastic constitutive model was developed to predict the heat build-up in rubbers during low cycle fatigue. The model was compared to the experiments using an example of a specimen subjected to tensile cyclic loading. The loading conditions, such as strain rates and strain amplitudes, were varied. The temperature dependence of the mechanical properties was not considered, as the surface temperature increase is not high. The model showed good agreement with the experimental results. Dippel et al. [8] performed different tests to investigate the time and temperature dependence of the mechanical properties of elastomers. A thermo-mechanical coupled material model based on the multiplicative decomposition of the deformation gradient into thermal and mechanical parts was developed. The effectiveness of the model was shown through experimental results of tension tests at different temperatures. Johlitz et al. [11] simplified this model [8] so that no thermal mechanical split of the deformation gradient is needed. The two models [8, 11] show the effect of the deformation amplitude and frequency on the heat dissipation behaviour of elastomers. Schröder et al. [25] performed numerical studies using a modified model of finite viscoelasticity to examine the dependence of the temperature profile on applied frequencies and amplitudes. Additionally, a parametric study was conducted to investigate the influence of boundary and initial conditions on the self-heating effect. The derivation and the implementation of the thermo-mechanically coupled material model as a user subroutine in Abaqus (UMAT) was discussed in [26].

Abdelmoniem and Yagimli [1] conducted numerical studies on the self-heating phenomenon and its effect on the applied loading conditions using a cylindrical sample subjected to a rotating shear load as an example. A thermo-mechanically coupled model, based on the suggested model by Simo and Hughes [28] for finite viscoelasticity, was implemented in Abaqus software. The temperature dependent viscosity was considered through the WLF (Williams–Landel–Ferry) equation [31]. The investigation demonstrated the impact of self-heating on the induced force due to viscoelasticity and how the thermal boundary conditions of the setup influenced the resulting forces. The simulated rotating shear loading in [1] was initially introduced by the experimental setup developed by Gent [9]. This type of loading introduces an out-of-phase force component due to

viscoelasticity, which affects fatigue life, as discussed by Klauke [13]. The out-of-phase force was simulated using the morph model by Juhre et al. [12] and by using the model of endochronic plasticity by Baaser et al. [3].

In this study, an experimental set-up is introduced to apply rotating shear load to cylindrical specimens. The surface temperature development is measured, and the effect of the self-heating phenomenon on the resulting forces is examined and discussed. A finite viscoelastic material model, based on the multiplicative decomposition of the deformation gradient, is used to describe the experimentally observed phenomena. The numerical analysis is like the one conducted by the authors in [1], except the material model used is more suitable in terms of thermodynamic consistency and other aspects concerning the physical responses of the used Maxwell elements. Those aspects were discussed in detail by Yagimli et al. [32]. This paper is structured as follows: In the first section, the experimental set-up is introduced, and the experimental measurements are shown and discussed. The second part presents the material model used in the study. In the third part, the simulation model is described, and the simulation results are discussed. Finally, a comparison between the simulation results and experiments is performed.

Experimental set-up and experimental results

For the application of the rotating shear load, the setup shown in Fig. 1 was implemented. The rubber specimen (1) was clamped between the upper and lower shafts using standard tool holding collets. The lower bearing block was fixed on a force sensor (3) capable of measuring forces in the radial, axial, and transverse directions, as well as resulting moments. Surface temperature was measured using the infrared sensor (2), and the number of rotations was counted using the photoelectric sensor (4). The experiment was performed in two steps. After clamping the sample, in the first step, the lower bearing block was displaced in the radial direction, subjecting the sample to simple shear deformation. In the second step, the motor was turned on, and the sample rotated at a speed adjusted by the speed adjustment knob (5). The sample was a standard rubber buffer made of natural rubber (NR) of shore hardness 55A. A drawing of the rubber sample is shown Fig. 2. In operation, these rubber buffers are designed to dampen shocks and isolate vibrations from machines. The contoured profile in the sample effectively reduces high loads during radial deflections, thereby increasing the component's lifespan.

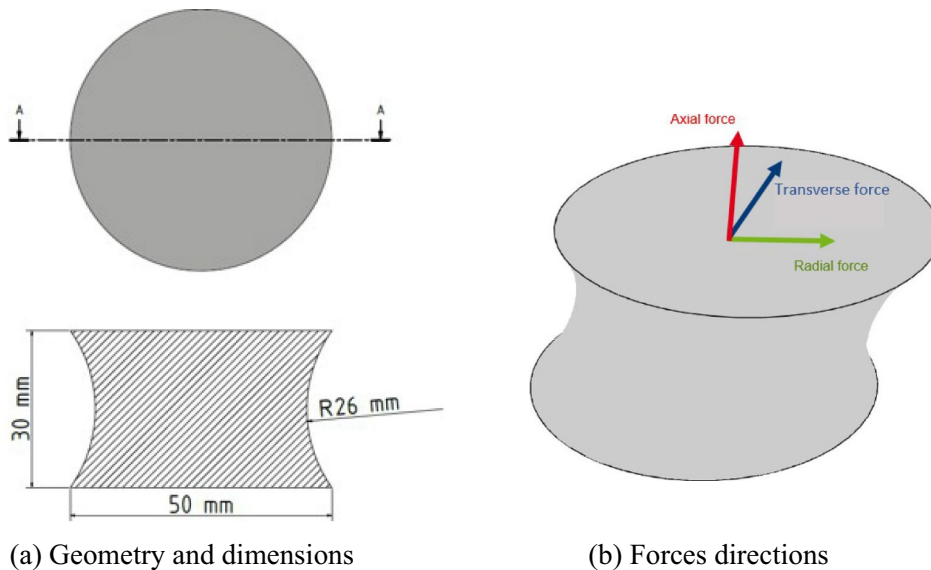
Fig. 1 Experimental set-up for rotating shear loading



- 1- Rubber specimen
- 2- Temperature sensor
- 3- Force sensor
- 4- Photoelectric sensor
- 5- Rotation speed adjustment

1

Fig. 2 Sample geometry (a) and the direction of the forces (b)



(a) Geometry and dimensions

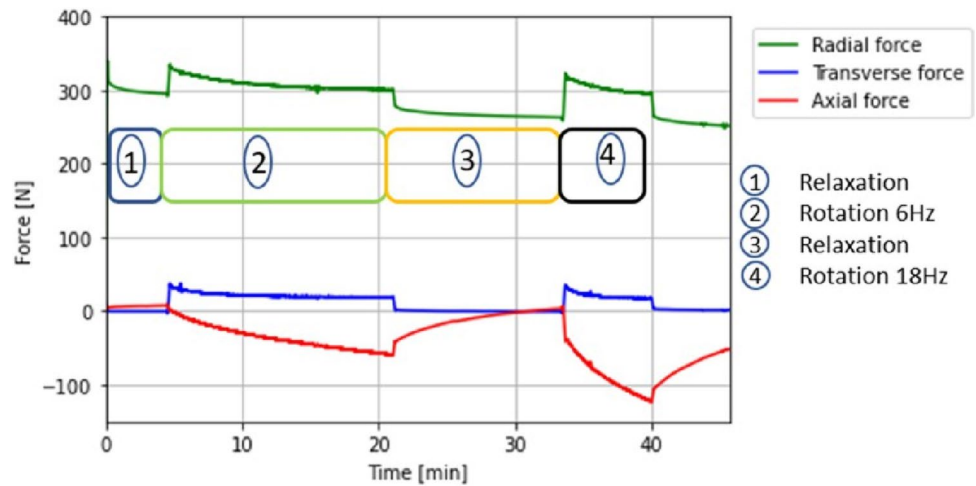
(b) Forces directions

Four steps loading experiment

In the first experiment, the loading was applied in four steps. In the first step, the specimen was deformed 6 mm in the radial direction and the radial force increased with deformation as shown in Fig. 3. The deformation was then kept constant, and the radial force relaxed with time. In the second step, the sample was rotated with a rotation frequency of $f = 6$ Hz. The radial force increased and due to

softening and temperature effects, it decreased with time. A force in the transverse direction was produced due to viscoelasticity. This force is only induced if the sample is rotated. In the axial direction, the axial force started to increase, causing a compression load on the bearing block due to the thermal expansion of the sample. The rotation was stopped in the third step of the experiment. The radial force continued to relax, and the transverse force disappeared as there was no rotation and no dissipation

Fig. 3 Forces development in the four-step loading experiment



occurred. As a result, the sample was left to cool in stationary air. The diminishing compression force on the bearing block indicates that the sample, upon cooling in still air, gradually regains its original shape.

In the last step, the rotation began with a higher frequency, this time $f = 18$ Hz. The radial force increased as the material responded with spontaneous elasticity. The transverse force was generated due to dissipation and with a higher rate of self-heating, thermal expansion occurred with a higher rate, causing the axial force to increase (increasing the compression on the bearing block).

In Fig. 4, the change in the surface temperature of the sample was recorded with time. In the first step of the test, no temperature change was observed as there was no cyclic loading and accordingly no dissipation. In the second step, the temperature began to increase and converge towards steady state. As soon as the rotation stopped in step 3, no heat generation took place, and the sample was left to cool down by natural convection. In the last step, the sample was

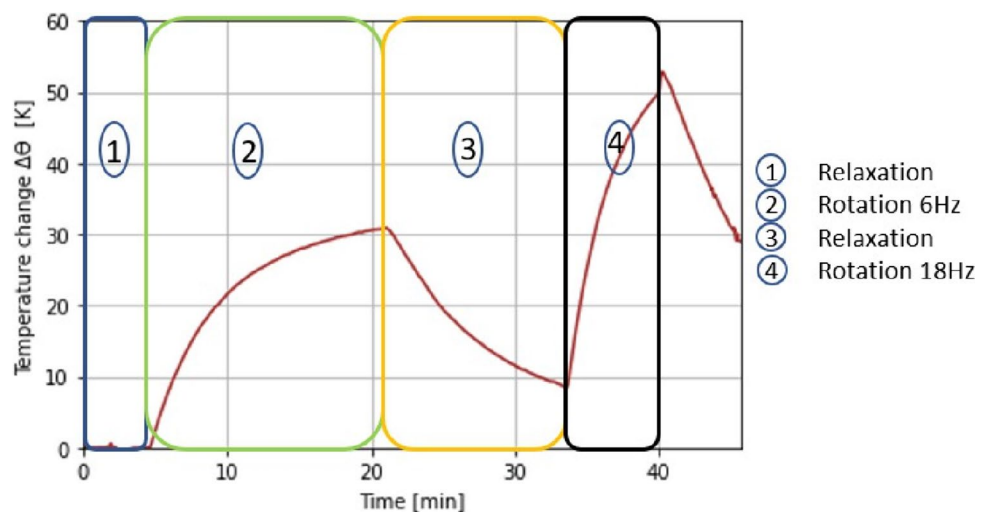
rotated, the heat generation started again with a higher rate and the surface temperature increased.

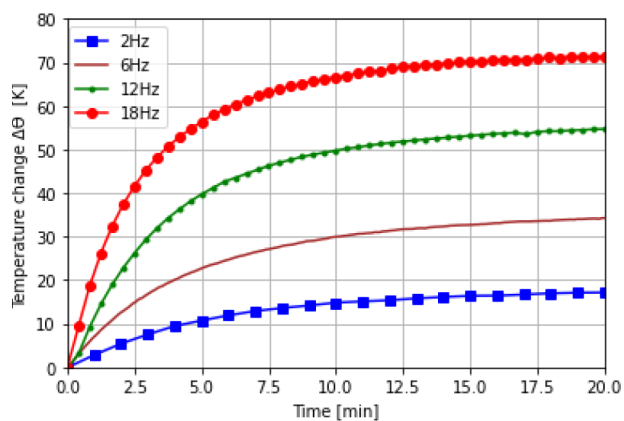
After the second rotation step had finished, a sudden increase of the surface temperature of around 4 K was observed. That was due to the change in the convective heat transfer coefficient from the rubber sample to air. When the sample was rotating at 18 Hz, the heat transfer by convection was higher compared to the case when there was no rotation. After stopping the rotation at 6 Hz, this sudden rise in temperature was not observed. The heat transfer coefficient to air in that case might be higher, but not high enough to cause this sudden increase of temperature.

Effect of the rotation frequency on the resulting forces and surface temperature

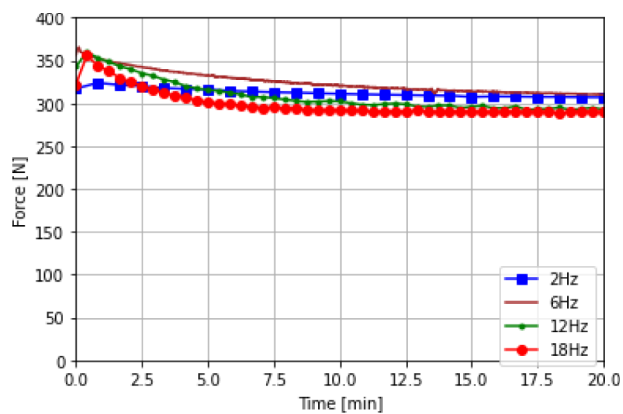
In order to study the effect of the rotation frequency on the resulting forces and surface temperature, the tests were performed with four rotation frequencies, 2, 6, 12 and 18 Hz. The surface temperature as well as the resulting radial,

Fig. 4 Surface temperature development in the four-step loading experiment

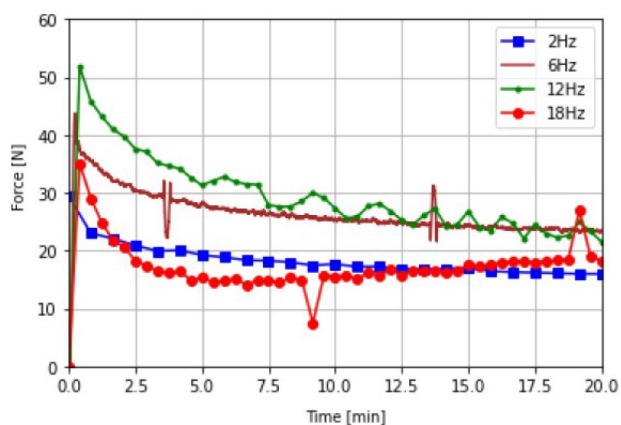




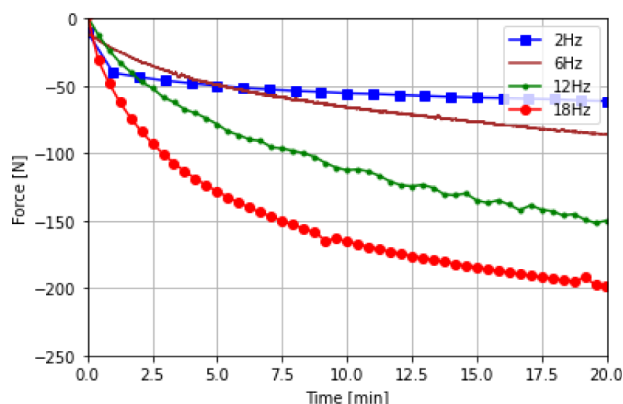
(a) Temperature change



(b) Radial force



(c) Transverse force



(d) Axial force

Fig. 5 The effect of changing the rotation frequency on the surface temperature, radial, transverse and axial forces

transverse and axial forces were measured. In Fig. 5a, the change in the steady state temperature with increasing the frequency is shown. As the frequency increased, the sample did not have enough time to cool down. The development of the radial forces at different frequencies is shown in Fig. 5b. At the steady state temperature, the force values for the different cases were near to each other, indicating that this frequency range did not affect the stiffness of the sample. However, it can be noticed that the rotated samples with higher frequencies were affected by the temperature rise. Both at 18 and 12 Hz, the radial force had a higher initial value and decreased due to the temperature effect. It can be concluded that the frequency had an indirect effect in this case on the sample stiffness.

The higher the frequency, the higher the temperature rise in the sample and the lower the sample stiffness which can be seen in the development of the radial forces. The same behaviour appeared for the transverse forces as shown in Fig. 5c. The high temperatures at 12 and 18 Hz influenced

the force development before reaching the steady state. At steady state temperature, the transverse force had similar values in the studied frequency range.

The most prominent effect of the frequency is shown on the axial forces as shown in Fig. 5d. The higher the frequency the larger the thermal strains and the compressive forces on the bearing block were higher due to the increase in the axial force. It should be also noticed that the values of the axial forces were affected by the temperature distribution along the sample. The measured surface temperature might reach a nearly steady state value, but the compressive axial force continued to increase, indicating that the heat transfers through the sample cross-section by conduction did not reach the steady state yet. In addition, the thermal properties of the material such as the convective heat transfer coefficient affected largely the temperature distribution across the sample and consequently the resulting thermal strain and axial forces.

The effect of the deformation amplitude on the resulting forces and surface temperature

To study the effect of the deformation amplitude on the dissipation behaviour, the deformation amplitude was lowered to half of its original value i.e., 3 mm instead of 6 mm. The results for the surface temperature are shown for both cases as in Fig. 6a.

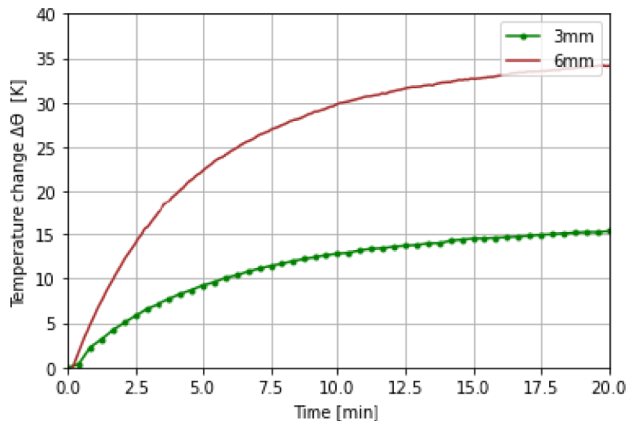
The radial forces were, as expected, higher in the case of 6 mm deformation. The temperature effect was also shown in the development of the radial force as it decreased until a steady state temperature was reached as shown in Fig. 6b. As the deformation increased, the dissipation increased, and the surface temperature rose. The dissipation induced transverse force was also larger in case of 6 mm deformation than that for 3 mm. In the beginning of the rotation step, the transverse force at 6 mm deformation was nearly double the value of the force at 3 mm. This force was then affected by

the temperature of the sample. It decreased with time, till a steady state was reached (Fig. 6c).

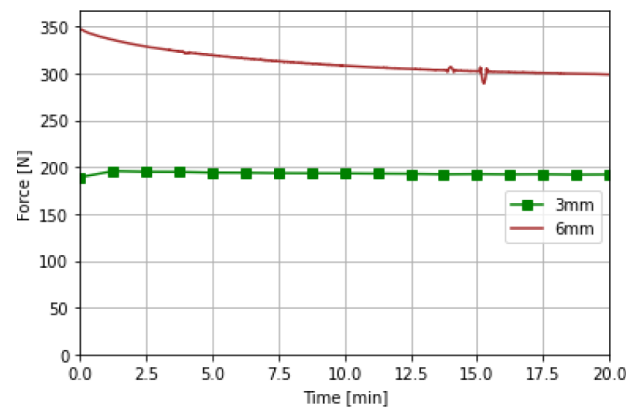
In case of the axial forces, due to the lower heat generation produced in the case of 3 mm deformation, the thermal strains and the compressive forces were less compared to the 6 mm deformation (Fig. 6d).

Summary of the experimental results

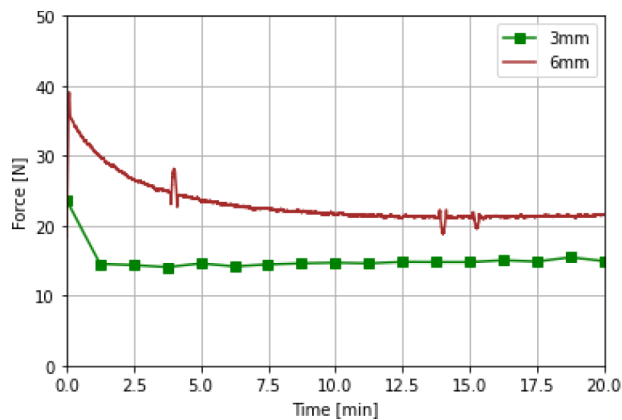
For each load case shown above, three tests were performed to ensure statistical validity. The mean values of the three tests were compared in a later section with the simulation results. As the rotation step started, a transverse force was generated as a result of the viscoelastic behaviour of the sample. This transverse force resulted in a dissipated mechanical work leading to a heat build-up in the sample. As the sample temperature increases, thermal strain occurred, and a compressive force was measured as shown in the



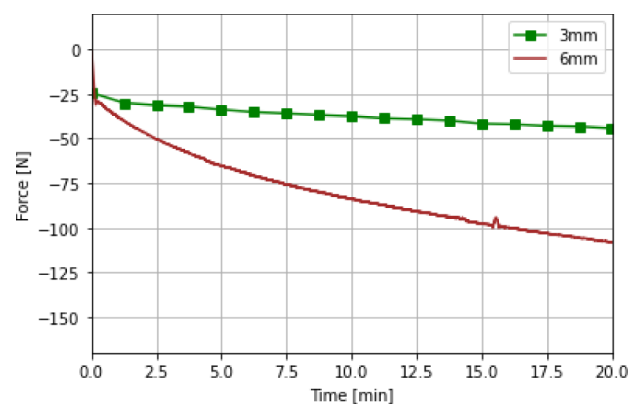
(a) Temperature change



(b) Radial force



(c) Transverse force



(d) Axial force

Fig. 6 Effect of changing the deformation amplitude on the surface temperature, radial, transverse and axial forces

development of the axial forces. The resulting forces in the radial, transverse and axial directions changed simultaneously with the changing temperature of the sample due to self-heating. For the modelling of the material behaviour under these loading conditions, a hyper-viscoelastic material model that includes heat dissipation, temperature dependency of material properties and thermal strains is needed. In the following section the used material model for the simulation is described.

Material model and material parameters

Kinematics of the model

To account for the thermal strains, the deformation gradient is firstly split into thermal and mechanical parts, viz.:

$$\mathbf{F} = \mathbf{F}_M \cdot \mathbf{F}_\theta. \quad (1)$$

The thermal part of the deformation gradient is defined as in Eq. (2), where α is the linear expansion coefficient and θ_0 is the reference temperature, which is set to 293 K.

$$\mathbf{F}_\theta = ((\alpha(\theta - \theta_0)) + 1)\mathbf{I}. \quad (2)$$

The mechanical part of the deformation gradient is split into isochoric and volumetric parts as follows:

$$\mathbf{F}_M = \bar{\mathbf{F}} \cdot \hat{\mathbf{F}}, \quad (3)$$

whereby the isochoric part is further split into an elastic $\hat{\mathbf{F}}_e$ and an inelastic part $\hat{\mathbf{F}}_i$ as in Eq. (4) as follows:

$$\hat{\mathbf{F}} = \hat{\mathbf{F}}_e \cdot \hat{\mathbf{F}}_i. \quad (4)$$

Definition of the Helmholtz free energy

The free energy is defined as an additive split of the equilibrium, non-equilibrium, volumetric and thermal part:

$$\rho_0 \Psi = \rho_0 \Psi_{eq}^{iso} + \sum_{j=1}^n \rho_0 \Psi_{nep}^j + \rho_0 \Psi_{eq}^{vol} + \rho_0 \Psi_{th}. \quad (5)$$

The volumetric part is defined as:

$$\rho_0 \Psi_{eq}^{vol} = \frac{1}{2} k (J_M - 1)^2, \quad (6)$$

where k is the bulk modulus of the material and J_M is the determinant of the mechanical deformation gradient in Eq. (3). For the description of the viscoelastic behaviour, the five-parameter model is used as shown in Fig. 7.

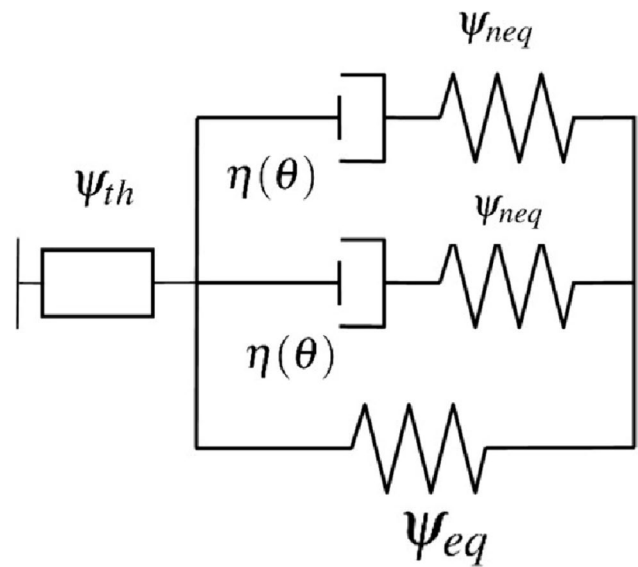


Fig. 7 Viscoelastic rheological model

For the equilibrium part of the free energy, Yeoh model is used:

$$\rho_0 \Psi_{eq}^{iso} = C_{10}(I_C - 3) + C_{20}(I_C - 3)^2 + C_{30}(I_C - 3)^3, \quad (7)$$

and for the springs of the Maxwell elements, the Neo-Hooke energy function is used:

$$\rho_0 \Psi_{neq} = C_{e10,1}(I_{Ce,1} - 3) + C_{e10,2}(I_{Ce,2} - 3). \quad (8)$$

The thermal part of the free energy is computed as follows:

$$\rho_0 \Psi_{th} = \rho_0 c \left((\theta - \theta_0) - \theta \ln \frac{\theta}{\theta_0} \right). \quad (9)$$

Calculation of the Cauchy stress tensor

The total Cauchy stress tensor is the sum of the equilibrium, non-equilibrium and volumetric stresses and is computed as the derivative of the free energy function with respect to the deformation.

$$\boldsymbol{\sigma} = \boldsymbol{\sigma}_{eq} + \sum_{j=1}^n \boldsymbol{\sigma}_{neq}^j + \boldsymbol{\sigma}_{vol}. \quad (10)$$

The equilibrium stress, after the transformation to the current configuration reads:

$$\boldsymbol{\sigma}_{\text{eq}} = \frac{1}{J} \left(2C_{10} + 4C_{20}(I_{\hat{\mathbf{B}}} - 3) + 6C_{30}(I_{\hat{\mathbf{B}}} - 3)^2 \right) \left(\hat{\mathbf{B}} - \frac{1}{3}I_{\hat{\mathbf{B}}}\mathbf{1} \right), \quad (11)$$

and the non-equilibrium:

$$\boldsymbol{\sigma}_{\text{neq}} = \sum_{j=1}^n \frac{2C_{e10}^j}{J} \left(\hat{\mathbf{B}}_e - \frac{1}{3}I_{\hat{\mathbf{B}}_e}\mathbf{1} \right), \quad (12)$$

where $\hat{\mathbf{B}} = \hat{\mathbf{F}} \cdot \hat{\mathbf{F}}^T$ is the mechanical isochoric left Cauchy–Green tensor, J is the determinant of the total deformation gradient \mathbf{F} and $\hat{\mathbf{B}}_e = \hat{\mathbf{F}} \cdot \hat{\mathbf{C}}_i^{-1} \cdot \hat{\mathbf{F}}^T$. The inelastic right Cauchy–Green tensor $\hat{\mathbf{C}}_i$ is to be determined by solving the following evolution equation [16] using the method introduced in Shutov et al. [27]:

$$\dot{\hat{\mathbf{C}}}_i = \frac{4C_{e10}}{\eta(\theta)} \left[\hat{\mathbf{C}}_i - \frac{1}{3} \text{tr}(\hat{\mathbf{C}} \cdot \hat{\mathbf{C}}_i^{-1}) \hat{\mathbf{C}}_i \right]. \quad (13)$$

The temperature influence on the viscosity is described using the WLF equation:

$$\eta(\theta) = \eta_0 \exp \left(- \frac{C_1(\theta - \theta_t)}{C_2 + \theta - \theta_t} \right), \quad (14)$$

where C_1 and C_2 are standard parameters of the WLF equation. The term η_0 is the viscosity at reference temperature θ_t . The volumetric stress is calculated as follows:

$$\boldsymbol{\sigma}_{\text{vol}} = \frac{k}{J_\theta} (J_M - 1) \mathbf{1}, \quad (15)$$

where J_θ is the determinant of the thermal deformation gradient in Eq. 2. The inelastic stress power is derived from the Clausius–Planck inequality and is calculated in the current configuration terms as follows:

$$D_m = \sum_{j=1}^n \frac{1}{\eta^j(\theta)} \boldsymbol{\sigma}_{\text{neq}}^j : \dot{\boldsymbol{\sigma}}_{\text{neq}}^j \geq 0. \quad (16)$$

The presented model in this section is a modified version of the model presented by Dippel et al. [8]. For the derivation of the dissipation function and the thermodynamical considerations of the model, the reader is referred to the following references [7, 8]. In literature, several formulations of the viscoelastic evolution equation and the dissipation function exist. For different formulations of the evolution equation, several non-Newtonian viscosity functions and their numerical treatment are compared together in a recent publication of Ricker et al. [23].

Abaqus implementation

The material model is implemented in the Abaqus Finite Element Method (FEM) software through a user material subroutine (UMAT). Once the stresses are defined, analytical derivations are carried out for the equilibrium (18) and volumetric (19) parts of the stresses. The non-equilibrium part of the tangent is obtained as outlined in references [15, 26], expressed by Eq. (20). The symbol \odot represents the symmetric 4th order dyadic product of two 2nd order tensors as in (17)

$$(A \odot B)_{ijkl} = \frac{1}{2} (A_{ik}B_{jl} + A_{il}B_{jk}). \quad (17)$$

$$\begin{aligned} \mathbb{C}_{eq}^4 = & 4 \left[\frac{\partial^2 \psi}{\partial I_{\hat{\mathbf{B}}} \partial I_{\hat{\mathbf{B}}}} \right] (\hat{\mathbf{B}} \otimes \hat{\mathbf{B}}) - \frac{4}{3} \left[\frac{\partial \psi}{\partial I_{\hat{\mathbf{B}}}} + \frac{\partial^2 \psi}{\partial I_{\hat{\mathbf{B}}} \partial I_{\hat{\mathbf{B}}}} \right] [(\hat{\mathbf{B}} \otimes \mathbf{1}) + (\mathbf{1} \otimes \hat{\mathbf{B}})] \\ & + \frac{4}{9} \left[\frac{\partial \psi}{\partial I_{\hat{\mathbf{B}}}} I_{\hat{\mathbf{B}}} + \frac{\partial^2 \psi}{\partial I_{\hat{\mathbf{B}}} \partial I_{\hat{\mathbf{B}}}} I_{\hat{\mathbf{B}}}^2 \right] (\mathbf{1} \otimes \mathbf{1}) + \frac{4}{3} \left[\frac{\partial \psi}{\partial I_{\hat{\mathbf{B}}}} I_{\hat{\mathbf{B}}} \right] (\mathbf{1} \odot \mathbf{1}) \end{aligned} \quad (18)$$

$$\mathbb{C}_{vol}^4 = J \left[\left[\frac{\partial \psi}{\partial J_m} + J \frac{\partial^2 \psi}{\partial J_m^2} \right] (\mathbf{1} \otimes \mathbf{1}) - \frac{2 \partial \psi}{\partial J_m} (\mathbf{1} \odot \mathbf{1}) \right] \quad (19)$$

$$\begin{aligned} \mathbb{C}_{neq}^4 = & \sum_{j=1}^n -\frac{4}{3} \left[\frac{\partial \psi}{\partial I_{\hat{\mathbf{B}}_e^j}} \right] [(\hat{\mathbf{B}}_e^j \otimes \mathbf{1}) + (\mathbf{1} \otimes \hat{\mathbf{B}}_e^j)] + \frac{4}{9} \left[\frac{\partial \psi}{\partial I_{\hat{\mathbf{B}}_e^j}} I_{\hat{\mathbf{B}}_e^j} \right] (\mathbf{1} \otimes \mathbf{1}) \\ & + \frac{4}{3} \left[\frac{\partial \psi}{\partial I_{\hat{\mathbf{B}}_e^j}} I_{\hat{\mathbf{B}}_e^j} \right] (\mathbf{1} \odot \mathbf{1}) \end{aligned} \quad (20)$$

In the context of UMAT, four tangent operators are defined for the thermo-mechanically coupled models. The mechanical tangent, denoted as DDSDE in Eq. (21), captures the mechanical response. The thermo-mechanical tangent, DDSDDT, is expressed as $\phi^* \left(\frac{\partial \mathbf{S}}{\partial \theta} \right)$, where \mathbf{S} represents the second Piola–Kirchhoff tensor, and $\phi^*(\cdot)$ denotes the push-forward operation to the current configuration. Additionally, the sensitivity of the heat source term R_{PL} with respect to deformation DRPLDE is defined as $\phi^* \left(\frac{\partial R_{PL}}{\partial \mathbf{C}} \right)$, and with respect to temperature DRPLDT as $\left(\frac{\partial R_{PL}}{\partial \theta} \right)$.

$$\mathbb{C} = \frac{1}{J} \left[\mathbb{C}_{eq}^4 + \mathbb{C}_{neq}^4 + \mathbb{C}_{vol}^4 \right] + [\mathbf{1} \odot \boldsymbol{\sigma}] + [\boldsymbol{\sigma} \odot \mathbf{1}] \quad (21)$$

For the implementation of thermo-mechanically coupled models and the derivation of tangent operators in UMAT, the reader is referred to the work of Yagimli [33], Ostwald et al. [18] and Schröder et al. [26].

Table 1 Material parameters for the simulation

Material parameters				
Parameter	Symbol	Value	Unit	
Hyperelasticity: Yeoh model				
Yeoh-Parameter 1	C_{10}	0.55	MPa	
Yeoh-Parameter 2	C_{20}	0.03	MPa	
Yeoh-Parameter 3	C_{30}	-0.0004	MPa	
Density	ρ_0	1.13×10^{-9}	tonne/mm ³	
Bulk modulus	k	1000	MPa	
Viscoelasticity				
Stiffness in the first Maxwell branch	C_{e10}^1	0.145	MPa	
Stiffness in the second Maxwell branch	C_{e10}^2	0.0042	MPa	
Viscosity in the first Maxwell branch	η_1	0.4804	MPas	
Viscosity in the second Maxwell branch	η_2	0.002	MPas	
WLF-parameter [26]				
Standard parameter 1	C_1	-16	-	
Standard parameter 2	C_2	-730	K	
Reference temperature	θ_t	296	K	
Thermal properties of rubber [25]				
Thermal conductivity	λ	0.328	mW/mm K	
Specific heat capacity	CP	1.639×10^9	mJ/t K	
Optimised specific heat capacity	CP, opt	1.639×10^7	mJ/t K	
Heat transfer [2, 10, 25]				
Convective heat transfer coefficient from rubber to steel	$\hat{\alpha}_{RS}$	0.1	mW/mm ² K	
Convective heat transfer coefficient from rubber to stationary air	$\hat{\alpha}_{RA}$	0.005	mW/mm ² K	
Steel emissivity	ϵ_s	0.2	-	
Rubber emissivity	ϵ_R	0.95	-	

Material parameters for the simulation

Relaxation tests under shear deformation were performed to obtain the hyperelastic parameters for the Yeoh model as well as the viscosities for the Maxwell arms. All other parameter such as bulk modulus and thermal properties

Table 2 Assumed convective heat transfer coefficient at different rotation frequencies

Convective heat transfer coefficient	
Frequency (Hz)	$\hat{\alpha}_{RA}$ (mW/mm ² K)
0	0.005
2	0.0083
6	0.15
12	0.25
18	0.35

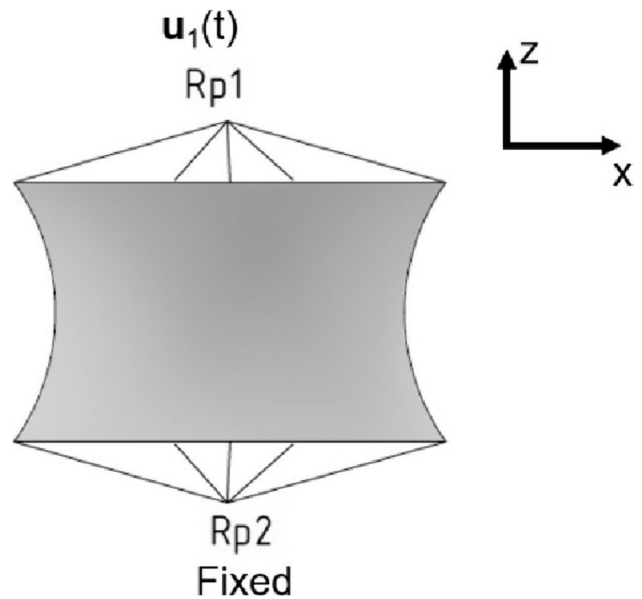
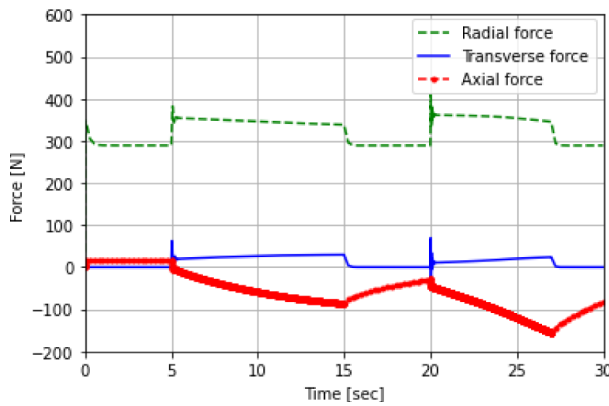
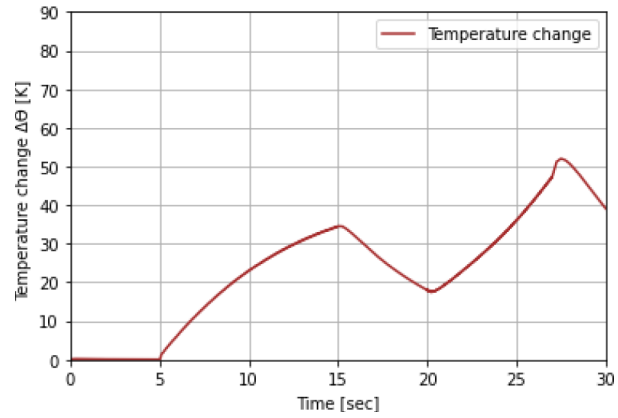


Fig. 8 Mechanical boundary conditions of the simulation



(a) Forces development



(b) Surface temperature

Fig. 9 Simulation results of the four steps loading experiment

were taken from literature values for natural rubber. It is important to highlight that the C_{30} of a negative value will lead to an unstable Yeoh model at large nominal strains. For the model stability at larger strains (more than 100%), the identification of the parameter C_{30} in the Yeoh model must adhere to the condition of being non-negative. Table 1 summarises the material parameter used for the simulation. The convective heat transfer is increased as the sample rotates at higher frequencies. The increase in that transfer is assumed to be linear to match the experimental observations. The assumed heat transfer coefficients for different frequencies are stated in Table 2. In order to reduce the simulation time for the different simulation cases, the specific heat capacity is reduced by a factor of 100 ($C_{P, opt}$). This will lead to shorter simulation time with no impact on the calculated steady state temperature [26].

Simulation boundary conditions and simulation results

Simulation of the four loading steps experiment

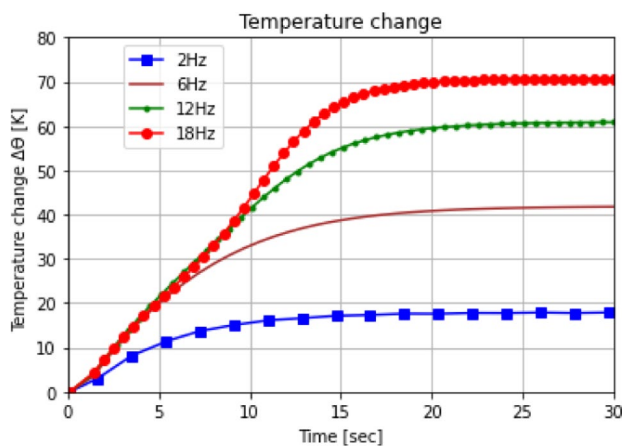
The capability of the model of displaying the experimental results was firstly checked by simulating the four loading steps experiment discussed in “Experimental set-up and experimental results” section. The sample was discretised with 3377 C3D8HT elements (8 nodes linear brick, coupled temperature displacement hybrid elements with constant pressure). The displacement boundary conditions were set as shown in Fig. 8. The upper and lower

surfaces of the sample were connected to remote points RP_1 and RP_2 , respectively. The remote point RP_2 was held fixed throughout the simulation and a displacement vector $\mathbf{u}_1(t) = [u_x(t), u_y(t), u_z(t)]^T$ was applied to RP_1 as in equation 22. The directions x, y and z represent the radial, transverse and axial directions.

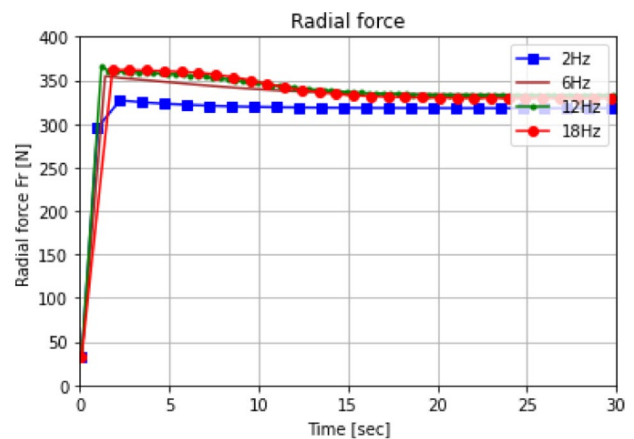
$$\mathbf{u}_1(t) = \begin{cases} \begin{bmatrix} 4u_1 t \\ 0 \\ 0 \end{bmatrix}, & 0 \leq t \leq 0.25s \\ \begin{bmatrix} u_1 \\ 0 \\ 0 \end{bmatrix}, & 0.25 < t \leq 5s \\ \begin{bmatrix} u_1 \cos(\omega_1 t) \\ u_1 \sin(\omega_1 t) \\ 0 \end{bmatrix}, & 5 < t \leq 15s \\ \begin{bmatrix} u_1 \\ 0 \\ 0 \end{bmatrix}, & 15 < t \leq 20s \\ \begin{bmatrix} u_1 \cos(\omega_2 t) \\ u_1 \sin(\omega_2 t) \\ 0 \end{bmatrix}, & 20 < t \leq 27s \\ \begin{bmatrix} u_1 \\ 0 \\ 0 \end{bmatrix}, & 27 < t \leq 30s \end{cases} \quad (22)$$

ω_1 and ω_2 are the angular rotation frequencies $\omega_1 = 2\pi f_1$ and $\omega_2 = 2\pi f_2$ where $f_1 = 6\text{Hz}$ and $f_2 = 18\text{Hz}$. u_1 is the applied deformation and is equal to 6 mm.

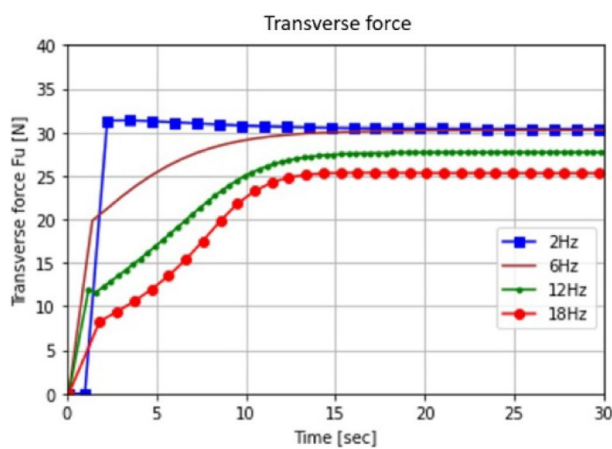
As shown in Fig. 9a, as soon as the rotation step started ($5 < t \leq 15$), the transverse force was induced and the surface temperature of the sample increased (Fig. 9b). The axial



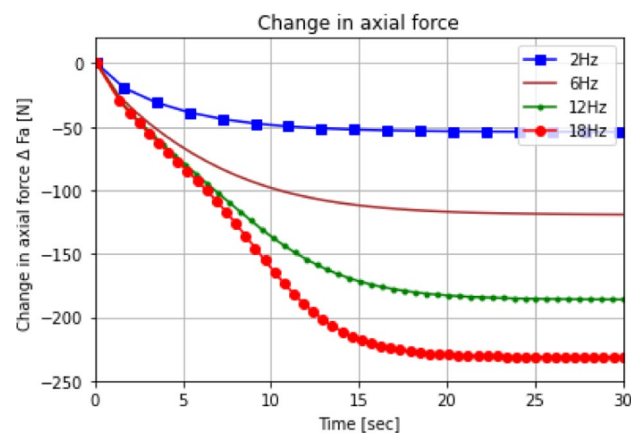
(a) Temperature change



(b) Radial force



(c) Transverse force



(d) Axial force

Fig. 10 Simulation results for the effect of changing the rotation frequency on the surface temperature, radial, transverse and axial forces

force (compressive force on the bearing block) increased with the increasing thermal strains due to continuous temperature rise along the sample cross section. As the rotation stopped ($15 < t \leq 20$), the induced transverse force disappeared, and the sample temperature decreased. The sample regained its original form before thermal strains and the axial force converged towards positive values. The second rotations step with $f = 18$ Hz ($20 < t \leq 25$) showed a higher rate of heat generation and consequently higher increase rate of the compressive force.

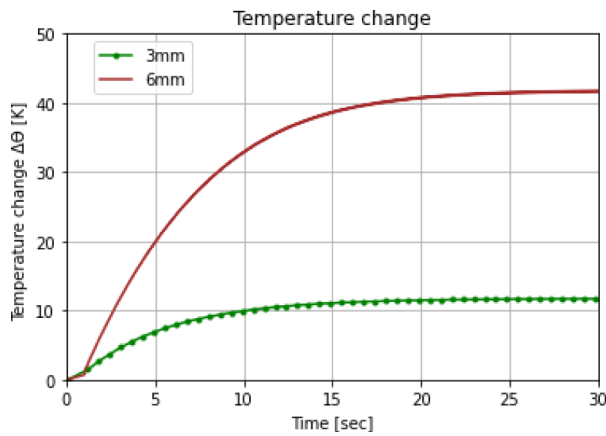
After the end of the second rotation step ($27 < t$), the sample was left to cool down in a stationary air which led to a lower heat convective heat transfer coefficient to air, and a sudden increase in the surface temperature could be displayed in Fig. 9b.

Changing the rotation frequency

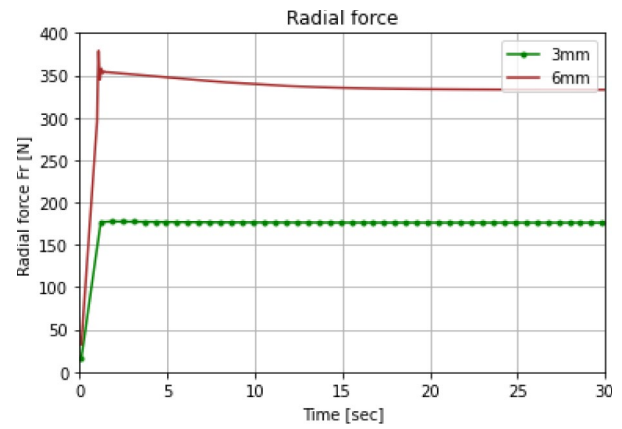
Using the same rotation frequencies set in the experiments, four simulations were performed. The boundary conditions in Eq. 22 were modified to include only two steps. The first step was the deformation step of 6 mm deformation. In the second step the rotation started for 30 seconds. The effect of changing the frequency on the surface temperature is shown in Fig. 10a.

The radial forces estimated at different frequencies are in the same range that was obtained by the experimental results. The effect of the temperature on the forces at 12 and 18 Hz can be shown (Fig. 10b).

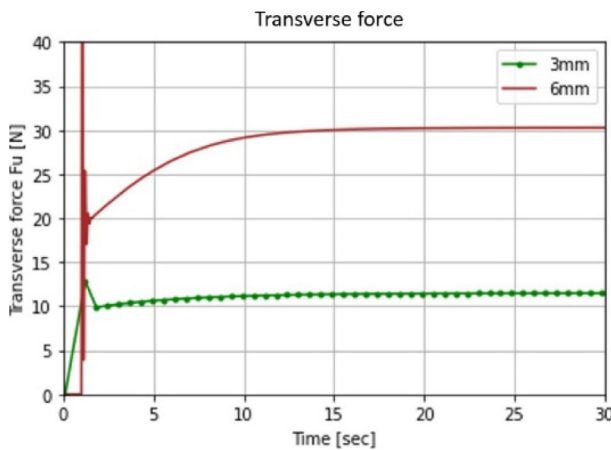
In the beginning of the development of the transverse forces a different progression was observed than the experimental results (Fig. 10c). This can be explained by the



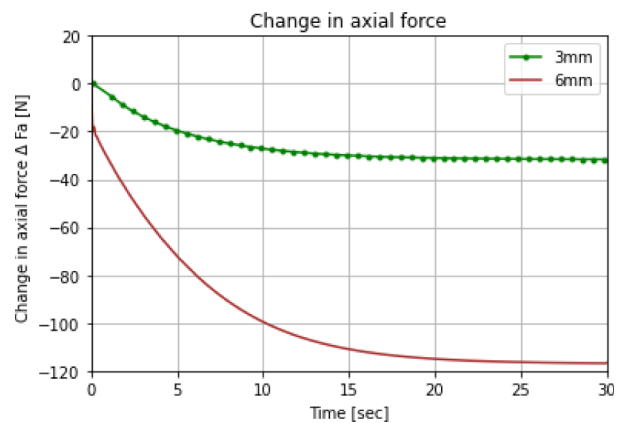
(a) Temperature change



(b) Radial force



(c) Transverse force



(d) Axial force

Fig. 11 Simulation results for the effect of changing the deformation amplitude on the surface temperature, radial, transverse and axial forces

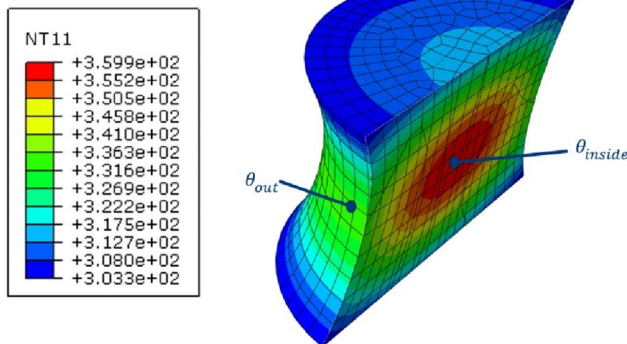


Fig. 12 Steady state temperature distribution along the sample at 6 mm shear deformation and a rotation frequency of 6 Hz. The shown results are in K

behaviour of the Maxwell elements used in the material model. The transverse forces are results of the dissipation process and describe the behaviour of the loss modulus of the material. Using only two Maxwell elements to model the viscoelastic behaviour appears to be insufficient. For the modelled material, the rotation frequency has very small effect on the value of the steady state in the studied frequency range (2, 6, 12 and 18 Hz). In order to estimate the transverse forces more accurately, dynamic mechanical analysis of the material is needed (DMA measurements) to estimate enough Maxwell elements that better describes the behaviour of the loss modulus and improve the simulation results for the transverse forces.

The change in the axial forces due to thermal strains agrees well with the obtained experimental values (Fig. 10d). It has to be noticed that the axial force is highly affected by the thermal properties of the material such as the thermal expansion coefficient, the convective

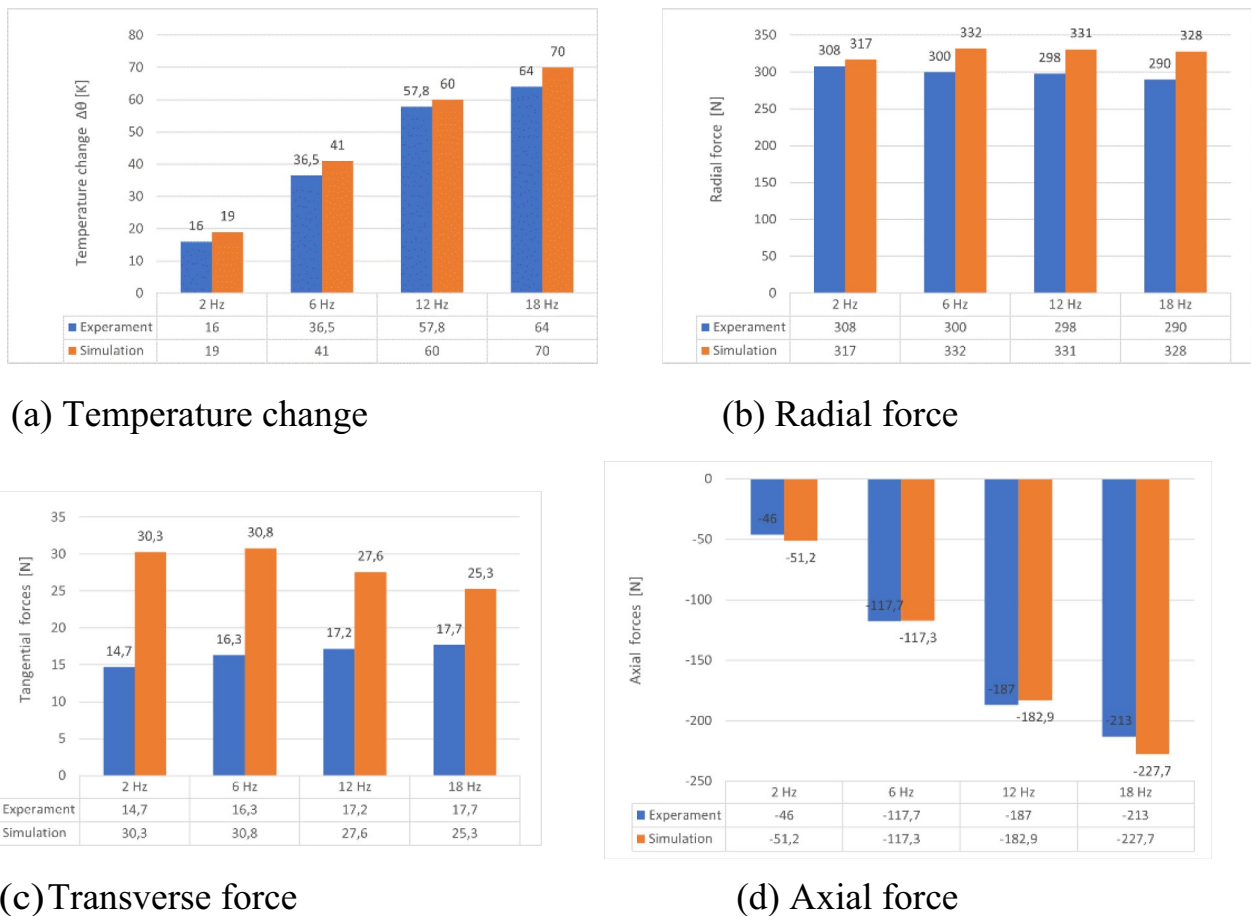


Fig. 13 Comparison between experimental and simulation results for the surface temperature, radial, transverse and axial forces

Table 3 Ratio of the transverse to the radial forces estimated experimentally and numerically

$F_{\text{transverse}}/F_{\text{radial}}$ (%)				
Frequency in (Hz)	2 Hz	6 Hz	12 Hz	18 Hz
Experiment	4.7	5.4	5.7	6.1
Simulation	9.5	9.2	8.3	7.7

heat transfer coefficient and the thermal conductance coefficient.

Changing the deformation amplitude

As shown in the experimental results, increasing the deformation amplitude result in increasing the dissipation and the heat build-up inside the material. The simulation results show the same behaviour of the experiments for the forces and temperature development. Fig. 11 shows the simulation results. For the simulation of larger deformation amplitudes (more than 6 mm), we recommended using material

models with viscosity functions that includes the deformation dependency.

Temperature distribution in the sample

The experimentally determined temperature was only measured at the outer surface of the sample. With the help of simulation results, the inner temperature of the sample can be estimated for the different loading conditions. In Fig. 12, the temperature distribution along the sample cross section was shown for the case of 6 mm deformation and a rotation frequency of 6 Hz.

These results show a temperature difference of about $\Delta\theta = \theta_{\text{out}} - \theta_{\text{inside}} = 24$ K. This high temperature gradient was caused by the low thermal conductivity of rubber and by the thermal boundary conditions used in the simulation such as the convective heat transfer coefficient from rubber to air ($\hat{\alpha}_{RA}$) and from rubber to steel ($\hat{\alpha}_{RS}$). In future work, we intend to measure the inside temperature of the sample to understand the influence of the temperature gradient on the development of the compressive force due to thermal strains.

Comparison to the experimental results

The mean values of the experimental results are compared to the simulation results as shown in Fig. 13. The simulation estimation of the change in the surface temperature, radial and axial forces followed the same behaviour and agreed well with the experimental results for all studied frequency ranges. The transverse force differed from the experimental results (Fig. 13c). Possible reasons were the use of two Maxwell elements in the material model, which might be insufficient in this case. The parameters for the WLF-equations are taken from literature which does not corresponds to the real behaviour of the material. The measured transverse force can be considered as a percentage value of the radial forces. In Table 3, the value of $F_{\text{transverse}}/F_{\text{radial}}$ is presented for the studied frequency range.

The transverse force is estimated to be around 7.7–9.5% of the radial forces. These values are slightly higher than the experimentally observed ones (4.7–6.1%). That explains why the estimation of the surface temperature is also slightly higher than the experimental values.

Conclusion

In this paper, the self-heating phenomena and its effect on the resulting forces during operation is tested using an experimental set up that applies a rotating shear load. The forces in radial, transverse directions are affected by the temperature rise due to self-heating. As the temperature of the sample increase, thermal strains occur, hence leading to axial forces. The axial forces increase with increasing the rotation frequency of the sample as a result of higher rate of heat generation. The experimentally observed phenomena are modelled using a modified material model for finite viscoelasticity. To account for thermal strains, the deformation gradient is split into thermal and mechanical parts. The model is implemented through user material subroutine (UMAT) in Abaqus software. Several simulations are performed, and the simulation results show the same behaviour and agree well with the experimental results in the applied frequency and deformation range. The simulation model, together with the introduced simple test rig can be used for the characterisation of rubber materials under wide range of deformation amplitudes and frequency ranges. The material model can be used to estimate the self-heating and the transfer function of rubber components during operation. In future work, the inner temperature of the sample will be measured and the temperature distribution across the sample cross section will be correlated with the development of the axial forces due to thermal

strains. With the accurate determination of the inner temperature of the sample through simulations, the thermal boundary conditions of the experimental set up can be adjusted to ensure homogeneous temperature distribution along the sample cross section. This can allow the use of the set-up for the execution of fatigue tests under different operating temperatures.

Acknowledgements The authors would like to specially thank Dipl.-Ing. Carsten Oppermann at Ostfalia University of Applied Sciences for his assistance in the lab-view programming tasks associated with the measurement units of the test rig.

Funding Open Access funding enabled and organized by Projekt DEAL.

Data availability The article contains all the data necessary for the results, and there is no need for additional source data.

Declarations

Conflict of interest The authors declare that they have no conflict of interest.

Open Access This article is licensed under a Creative Commons Attribution 4.0 International License, which permits use, sharing, adaptation, distribution and reproduction in any medium or format, as long as you give appropriate credit to the original author(s) and the source, provide a link to the Creative Commons licence, and indicate if changes were made. The images or other third party material in this article are included in the article's Creative Commons licence, unless indicated otherwise in a credit line to the material. If material is not included in the article's Creative Commons licence and your intended use is not permitted by statutory regulation or exceeds the permitted use, you will need to obtain permission directly from the copyright holder. To view a copy of this licence, visit <http://creativecommons.org/licenses/by/4.0/>.

References

1. Abdelmoniem M, Yagimli B (2021) Numerical studies on the heat dissipation process in elastomers under rotating loading direction. *J Rubber Res* 24(5):797–805
2. Banic Milan S et al (2012) Prediction of heat generation in rubber or rubber-metal springs. *Therm Sci* 16(suppl. 2):527–539
3. Baaser H, Heining C (2015) Application of endochronic plasticity on simulation of technical rubber components. *KGK Kaut Gummi Kunstst* 68(6):90–92
4. Behnke R, Kaliske M, Klüppel M (2016) Thermo-mechanical analysis of cyclically loaded particle-reinforced elastomer components: experiment and finite element simulation. *Rubber Chem Technol* 89(1):154–176
5. Boukamel A et al (2001) A thermo-viscoelastic model for elastomeric behaviour and its numerical application. *Arch Appl Mech* 71:785–801
6. Cruanes C et al (2019) Modeling of the thermomechanical behavior of rubbers during fatigue tests from infrared measurements. *Int J Fatigue* 126:231–240
7. Dippel B (2015) Experimentelle charakterisierung, modellierung und FE-berechnung thermomechanischer kopplung. Diss Phd thesis, Universität der Bundeswehr München

8. Dippel B, Johlitz M, Lion A (2015) Thermo-mechanical couplings in elastomers: experiments and modelling. *ZAMM J Appl Math Mech/Z Angew Math Mech* 95(11):1117–1128
9. Gent AN (1960) Simple rotary dynamic testing machine. *Br J Appl Phys* 11(4):165
10. He H et al (2022) Heat build-up and rolling resistance analysis of a solid tire: experimental observation and numerical simulation with thermo-mechanical coupling method. *Polymers* 14(11):2210
11. Johlitz M, Dippel B, Lion A (2016) Dissipative heating of elastomers: a new modelling approach based on finite and coupled thermomechanics. *Continuum Mech Thermodyn* 28:1111–1125
12. Juhre D et al (2011) Some remarks on influence of inelasticity on fatigue life of filled elastomers. *Plast Rubber Compos* 40(4):180–184
13. Klauke DIR (2016) Lebensdauervorhersage mehrachsiger belasteter elastomerbauteile unter besonderer Berücksichtigung rotierender beanspruchungsrichtungen
14. Kraus G (1984) Mechanical losses in carbon-black-filled rubbers. *J Appl Polym Sci Appl Polym Symp* 39:75
15. Lefevre V, Sozio F, Lopez-Pamies O (2024) Abaqus implementation of a large family of finite viscoelasticity models. *Finite Elem Anal Des* 232:104114
16. Lion A (1997) A physically based method to represent the thermo-mechanical behaviour of elastomers. *Acta Mech* 123(1–4):1–25
17. Mars William V et al (2021) Incremental, critical plane analysis of standing wave development, self-heating, and fatigue during regulatory high-speed tire testing protocols. *Tire Sci Technol* 49(3):172–205
18. Ostwald R, Kuhl E, Menzel A (2019) On the implementation of finite deformation gradient-enhanced damage models. *Comput Mech* 64:847–877
19. Pesek L, Pust L, Sulc P (2007) FEM modeling of thermo-mechanical interaction in pre-pressed rubber block. *Eng Mech* 14(1):2
20. Peter O, Stoczek R, Kratina O (2022) Experimental and numerical description of the heat build-up in rubber under cyclic loading. *Degradation of elastomers in practice, experiments and modeling*. Springer, Cham, pp 121–141
21. Reese S, Govindjee S (1998) A theory of finite viscoelasticity and numerical aspects. *Int J Solids Struct* 35(26–27):3455–3482
22. Rennar N, Decker A, Heinz M (2012) Heat-build-up und ultimate mechanische Eigenschaften von gefüllten elastomerwerkstoffen. *KGK Kaut Gummi Kunstst* 65(4):50–56
23. Ricker A, Gierig M, Wriggers P (2023) Multiplicative, non-Newtonian viscoelasticity models for rubber materials and brain tissues: numerical treatment and comparative studies. *Arch Comput Methods Eng* 30:1–39
24. Rodas CO, Zairi F, Nait-Abdelaziz M (2014) A finite strain thermo-viscoelastic constitutive model to describe the self-heating in elastomeric materials during low-cycle fatigue. *J Mech Phys Solids* 64:396–410
25. Schröder J, Lion A, Johlitz M (2021) Numerical studies on the self-heating phenomenon of elastomers based on finite thermo-viscoelasticity. *J Rubber Res* 24:237–248
26. Schröder J, Lion A, Johlitz M (2019) On the derivation and application of a finite strain thermo-viscoelastic material model for rubber components. *State Art Fut Trends Mater Model* 2019:325–348
27. Shutov Alexey V, Landgraf R, Ihlemann J (2013) An explicit solution for implicit time stepping in multiplicative finite strain viscoelasticity. *Comput Methods Appl Mech Eng* 265:213–225
28. Simo JC, Hughes TJ (2006) *Computational inelasticity*, vol 7. Springer, London
29. Stoczek R, Stenicka M, Kipscholl R (2019) Heat build-up characterization under realistic load. In: *Constitutive models for rubber XI proceedings of the 11th European conference on constitutive models for rubber*. CRC Press/Balkema, Nantes
30. Werner P, Baaser H (2021) Simulation of a heat-buildup process on rubber components. *KGK Kaut Gummi Kunstst* 74(3):43–47
31. Williams Malcolm L, Landel RF, Ferry JD (1955) The temperature dependence of relaxation mechanisms in amorphous polymers and other glass-forming liquids. *J Am Chem Soc* 77(14):3701–3707
32. Yagimli B, Lion A, Abdelmoniem MA (2023) Analytical investigation of the finite viscoelastic model proposed by Simo: critical review and a suggested modification. *Contin Mech Thermodyn* 2023:1–22
33. Yagimli B (2013) *Kontinuumsmechanische betrachtung von aushärtevorgängen: experimente, thermomechanische materialmodellierung und numerische umsetzung*. Verlag Dr, Hut

Publisher's Note Springer Nature remains neutral with regard to jurisdictional claims in published maps and institutional affiliations.